Eur. Phys. J. Special Topics **224**, 355–368 (2015)

DOI: 10.1140/epjst/e2015-02365-3

THE EUROPEAN PHYSICAL JOURNAL SPECIAL TOPICS

Regular Article

Experimental investigation of thermal structures in regular three-dimensional falling films

M. Rietz[1], W. Rohlfs[1,a], R. Kneer[1], and B. Scheid[2]

[1] Institute of Heat and Mass Transfer, RWTH Aachen University, Augustinerbach 6, 52056 Aachen, Germany
[2] TIPs, Université libre de Bruxelles, Avenue F. Roosevelt 50, 1050 Bruxelles, Belgium

Received 22 July 2014 / Received in final form 16 February 2015
Published online 8 April 2015

Abstract. Interfacial waves on the surface of a falling liquid film are known to modify heat and mass transfer. Under non-isothermal conditions, the wave topology is strongly influenced by the presence of thermocapillary (Marangoni) forces at the interface which leads to a destabilization of the film flow and potentially to critical film thinning. In this context, the present study investigates the evolution of the surface topology and the evolution of the surface temperature for the case of regularly excited solitary-type waves on a falling liquid film under the influence of a wall-side heat flux. Combining film thickness (chromatic confocal imaging) and surface temperature information (infrared thermography), interactions between hydrodynamics and thermocapillary forces are revealed. These include the formation of rivulets, film thinning and wave number doubling in spanwise direction. Distinct thermal structures on the films' surface can be associated to characteristics of the surface topology.

1 Introduction

Thin liquid layers or films are wall-bounded flows running down a vertical or inclined wall with a deformable liquid-gas interface. Those gravity driven flows are used in various applications such as cooling of mechanical or electronic systems, chemical processing, desalination and food processing [1,10], allowing for high heat transfer rates. Under non-isothermal conditions, the wave topology is strongly influenced by thermocapillary interfacial forces (called Marangoni forces) which lead to a destabilization of the flow and to the appearance of rivulets [13,20]. Undesired phenomena such as film rupture might occur, possibly overheating temperature-sensitive fluids or even damaging the heater.

Regular excited three-dimensional surface waves containing synchronously deformed fronts, subharmonic patterns and horseshoe-like waves [20] have been experimentally investigated by Park et al. [15], providing clear pictures of the wave

[a] e-mail: rohlfs@wsa.rwth-aachen.de

topology which resulted from a synchronous excitation. With a spatial excitation in spanwise direction and a temporal disturbance in streamwise direction, regular three-dimensional waves were obtained. The same approach of exciting the film flow was followed in earlier studies by the authors, where the influence of electric fields with and without additional heating was studied experimentally [17,18]. The advantage of regular three-dimensional waves is their streamwise and spanwise periodicity and symmetry, which allows for a direct comparison to three-dimensional numerical simulations. In Dietze et al. [6], a detailed numerical investigation of flow structures in laminar falling films (for four different flow conditions) has been performed using direct numerical simulations as well as a weighted integral boundary layer model [21]. The numerical results reveal that the flow field can be segregated into two regions: an inertia dominated region containing large wave humps (with a local Reynolds number that reaches up to five-fold the mean value), and a visco-capillary region, where capillary and/or viscous forces dominate [6].

In falling liquid films under non-isothermal conditions, the coupled thermocapillary and surface-wave instabilities enhance surface deformations leading to an array of rivulets in vertical direction [7,16]. These thermocapillary instabilities are known to induce film rupture, causing a self amplifying film thinning process in regions of high surface temperature.

Experimental investigation of thin films falling down locally heated plates have been performed by Kabov [8,9], revealing rivulet structures, horizontal bumps and lateral waves. In Lel et al. [13], regular structures in uniformly heated films have been observed for the case of natural surface waves. The experiments showed the formation of rivulets with an almost regular spacing, as predicted numerically by Scheid et al. [20] using a weighted integral boundary layer model.

In the present study, the evolution of regular excited surface waves under non-isothermal conditions is experimentally studied. In addition to the prior study of Rohlfs et al. [18], infrared thermography measurements were performed, revealing the interfacial temperature distribution of the liquid film. Furthermore, extended film thickness measurements depict the development of the surface topology throughout the streamwise and spanwise expansion of the employed heated section. These combined measurements allow to identify interactions of wave dynamics and thermal instabilities for a case of three-dimensional solitary type surface waves. High symmetry in the experimental data explicitly qualifies the shown results for comparison to and validation of related numerical simulations of non-isothermal falling film flows subject to regular artificial perturbations.

2 Experimental setup and experimental methods

Experimental setup

The experimental setup used in the present study has been applied before to investigate the effect of electrostatic surface forces on three-dimensional falling liquid films [18] as well as in Rohlfs et al. [17], where in addition the effect of thermocapillary forces has been studied. The setup is schematically shown in Fig. 1 and shall be recalled briefly.

The circulating working fluid (in this case silicon oil, DMS T12) is distributed through an adjustable blade onto the 150 mm wide test section, wherein a variable streamwise disturbance is imposed by an upstream loudspeaker mounted on top of the upper reservoir (see for a similar excitation method Nosoko et al. [14]), superimposing the natural inherent noise of the system. The observed streamwise wavelength

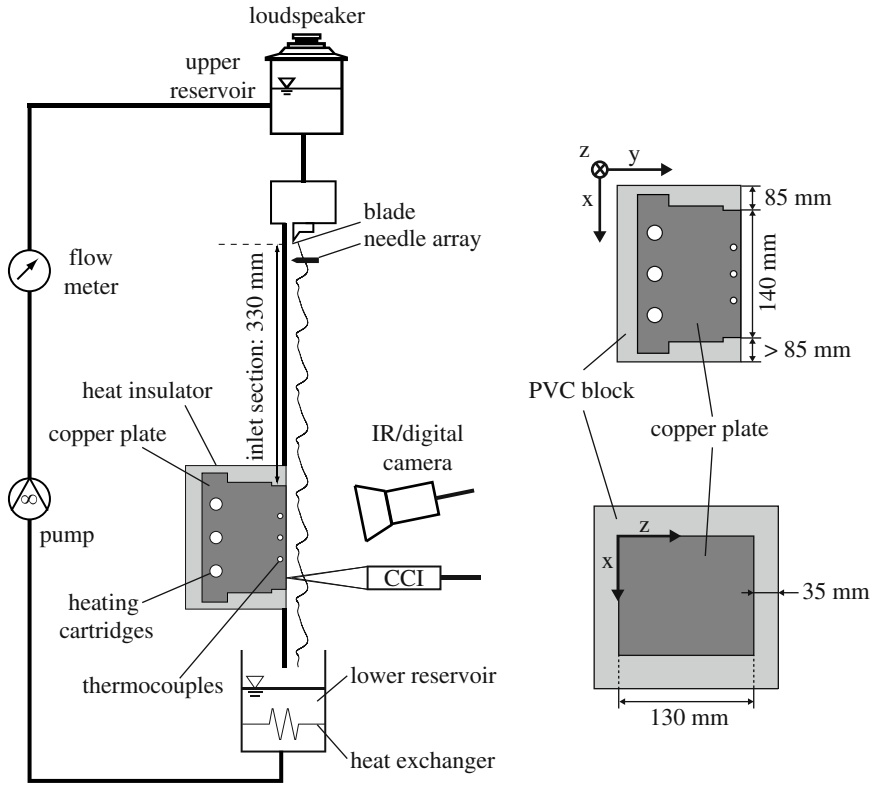

Fig. 1. Experimental setup.

Λ_x depends on this imposed frequency and on the wave propagation, which is controlled through the flow rate. At a distance of 20 mm downstream, an additional spanwise wavelength is directly imposed by five equidistant needles. In this context, a wavelength of $\Lambda_z = 30$ mm was found to approximately coincide with the maximal amplified spanwise perturbation and consequently employed in the presented experiments. For $\Lambda_z < 20$ mm and $\Lambda_z > 35$ mm the high symmetry of the three-dimensional wave topology was lost. The entire test section consists of an unheated, 245 mm long vertical steel plate, which is followed in streamwise direction by a PVC (Polyvinyl Chloride) block (thermal conductivity: 0.20 W/mK) surrounding a heated copper plate. The copper plate with a length of 140 mm is mounted in the hydrodynamically established region (330 mm downstream the distribution gap). A reservoir collects the fluid at the end of the test section, where a heat exchanger cools down the liquid to a constant inlet temperature. A controlled piston pump transports the fluid from the lower to the upper reservoir, where the flow rate is measured (under steady state conditions) by a positive displacement flow meter with an accuracy of $\pm 0.3\%$.

The wall-side heat flux is imposed by heating cartridges embedded in a thick copper plate as depicted in Fig. 1. A regulated voltage supply source allows for a variation of the average heat flux between zero and 3 W/cm^2. The copper block is surrounded by a block of PVC acting as a thermal insulation. The temperatures within the heater are measured by multiple thermocouples at a distance of 6 mm from the surface. An analytical approximation of the instationary two-dimensional heat transfer problem for the investigated case has shown, that the difference between the measured temperature and the temperature at the wall is of the order of 0.01 K. Thus, the uncertainty

of the wall temperature measurement is approximately equal to the uncertainty of the measurement method (thermocouple), which is about $\pm 1\,\mathrm{K}$. The oscillations of the wall temperature are found to be of the order of $2 \times 10^{-4}\,\mathrm{K}$, fulfilling a constant temperature boundary condition. This simplifies the corresponding boundary condition in theoretical analysis, as detailed in Trevelyan et al. [22].

Chromatic confocal imaging

The liquid film thickness was measured using a chromatic confocal imaging (CCI) technique which was developed by Cohen-Sabban et al. [3] and previously used with falling liquid films [4,5,12,23] as well as in the previously mentioned studies [17,18] where the measurement principle is described in more detail.

The measurement error due to the film surface curvature has been investigated by Rohlfs et al. [18]. Validation measurements of a spherical object have been performed depicting good agreement up to an inclination of 23 degrees. The long wave nature of the hydrodynamic instability ensures the surface slope to remain, most of the time, within this range of inclination, for which the optical probe (IFS 2401-3) allows for an axial resolution of $0.12\,\mu\mathrm{m}$ and a lateral resolution of $25\,\mu\mathrm{m}$ in a measurement range of 3 mm.

In the conducted experiments, the wall distance y_w was measured from the dry wall before each measurement series. During the series, the position of the measurement device was fixed. Consequently, the film thickness δ_f was evaluated by $\delta_\mathrm{f} = y_\mathrm{w} - y_\mathrm{f}$, where y_f is the measured position of the film surface (liquid-gas interface). To account for the thermal expansion of the copper plate, its expansion normal to the wall was measured for different temperatures. An average value of $2.4\,\mu\mathrm{m\,K^{-1}}$ was measured and used for correction.

Due to the highly three-dimensional interaction of hydrodynamics and thermocapillary instabilities, the three-dimensional topology of the film is reconstructed for a more detailed analysis. Hereby, the good reproducibility of the excited waves allows for a reconstruction by using consecutive spanwise point measurements (step size 0.25 mm). These spanwise point measurements were averaged over 30 successive wavelengths in order to obtain a representative temporal evolution of the film topology. The temporal displacement between subsequent point measurements is adjusted by a synchronization of the loudspeaker signal to the chromatic confocal imaging device. A weighted moving average filter was applied after the alignment in spanwise direction.

Note, that the result of the reconstruction is a wave with two spatial dimensions (height and spanwise position) and one temporal dimension, since the development of the film topology is evaluated at a single respective streamwise position. Only for the case of a constant wave velocity, the temporal development of the film thickness can be transformed to a spatial development according to $x = c\,t$, where c is the wave celerity. However, this transformation is not applicable in the region of interest, where the wave celerity changes (even with a spanwise varying gradient).

Infrared thermography

Infrared (IR) thermography was applied to determine the surface temperature field of the liquid film, using a camera with a mercury cadmium telluride detector in a spectral range of 7.7–$9.5\,\mu\mathrm{m}$ (Cedip JADE 3-LW). The surface temperature was recorded with a lateral resolution of 320×240 pixels at a frame rate of 240 Hz and an integration time of $305\,\mu\mathrm{s}$. The sensitivity of the IR camera is given according to the manufacturer with 21 mK at room temperature ($20\,^\circ\mathrm{C}$).

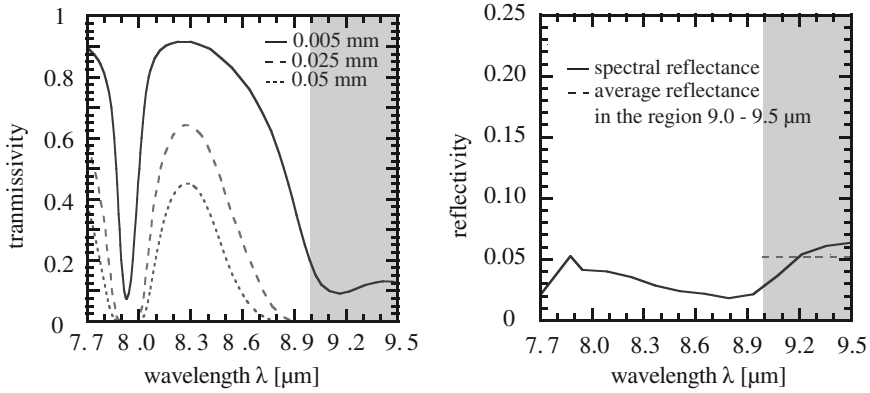

Fig. 2. Transmissivity and reflectivity of the employed silicon oil in the spectral range of the IR camera adopted from [11]. Transmissivity shown for different liquid layer thicknesses. Grey background: spectral range of the applied filter.

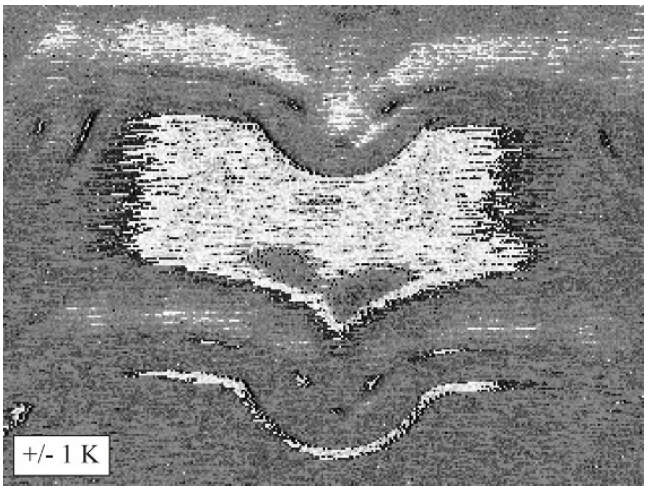

Fig. 3. IR image of the isothermal film with a surface wave forced in streamwise and spanwise direction, showing deviations due to the surface curvature of the film and inherent noise of the IR camera. The color-range from white to black corresponds to a temperature difference of 2 K.

The spectral transmissivity of the employed silicon oil is shown in Fig. 2 for different thicknesses (see also [12]). For wavelengths above 9 μm, the transmissivity is close to zero for a fluid layer thickness of 25 μm. For lower wavelengths, the transmissivity increases rapidly, for which a filter was applied limiting the spectral range to 9–9.5 μm. Consequently, only the heat radiation of a very thin layer of approximately 25 μm close to the surface is measured, which we will refer to as the surface temperature.

The average reflectance of the silicon oil in the given spectral range is about 5% (Fig. 2, right), such that hot objects in the environment might cause reflections on the film surface, disturbing the measurement. To reduce these disturbances, environmental radiation was blocked by a black curtain.

IR measurements were conducted at the bottom part of the heater (95–130 mm downstream the onset of heating). The error due to inherent noise of the detector and the surface curvature of the film was evaluated without heating at ambient temperature (see Fig. 3). Deviations of approximately 30 digital level were found,

Table 1. Experimental conditions.

control parameters		
inlet flow rate per unit length q	$[\mathrm{m^2 s^{-1}}]$	$7.43 \cdot 10^{-5}$
streamwise excitation f	[Hz]	12
spanwise excitation Λ_z	[mm]	30
copper plate temperature T_w	[°C]	70
ambient temperature T_∞	[°C]	20
fluid inlet temperature T_0	[°C]	21.7
fluid properties* at $T = 25\,^\circ\mathrm{C}$		
ρ	$[\mathrm{kgm^{-3}}]$	949
ν	$[\mathrm{m^2 s^{-1}}]$	$1.65 \cdot 10^{-5}$
σ	$[\mathrm{Nm^{-1}}]$	$20.6 \cdot 10^{-3}$
$\frac{d\sigma}{dT}$	$[\mathrm{N(Km)^{-1}}]$	$-6.7 \cdot 10^{-5}$
λ	$[\mathrm{W(mK)^{-1}}]$	0.145
c_p	$[\mathrm{J(kgK)^{-1}}]$	1546
dimensionless numbers		
Re	$q\nu^{-1}$	4.5
Pr	$\nu\rho c_p \lambda^{-1}$	167
Ka	$\sigma\rho^{-1} g^{-1/3} \nu^{-4/3}$	23.8
Ma	$-\frac{d\sigma}{dT}(T_w - T_\infty)\rho^{-1} g^{-1/3} \nu^{-4/3}$	3.87

*Fluid properties taken from Lel [11].

which correspond to maximal deviations in the measured temperature of 2 K at room temperature level. These deviations in digital level are most certainly associated to reflections between wave hump and residual layer and the varying orientation of the surface to the viewing direction of the IR-camera and will remain of the same magnitude for higher fluid temperatures. Note, that film thickness measurements and surface temperature measurements were not conducted simultaneously.

3 Results

From various flow conditions experimentally investigated, a case which is characterized by a distinct residual layer and solitary-type wave has been chosen for a detailed examination. The values of the dimensional and dimensionless parameters are presented in Table 1.

3.1 Evolution of wave topology

In the case of solitary waves, the topology of the regularly excited liquid film is characterized by a distinct residual layer, interrupted by steep isolated wave fronts. This wave topology is shown in Fig. 4 through time traces measured at three different spanwise positions and two different streamwise positions as labelled in the digital photography of the film surface. The photography also depicts the development of the wave front (or wave crest) over the expansion of the heated section. The spanwise symmetry is a result of the employed excitation mechanism, e.g. the submerged needles.

For the isothermal case, the initial shape of the wave front persists through the entire measurement section (not shown). Under non-isothermal conditions, with a

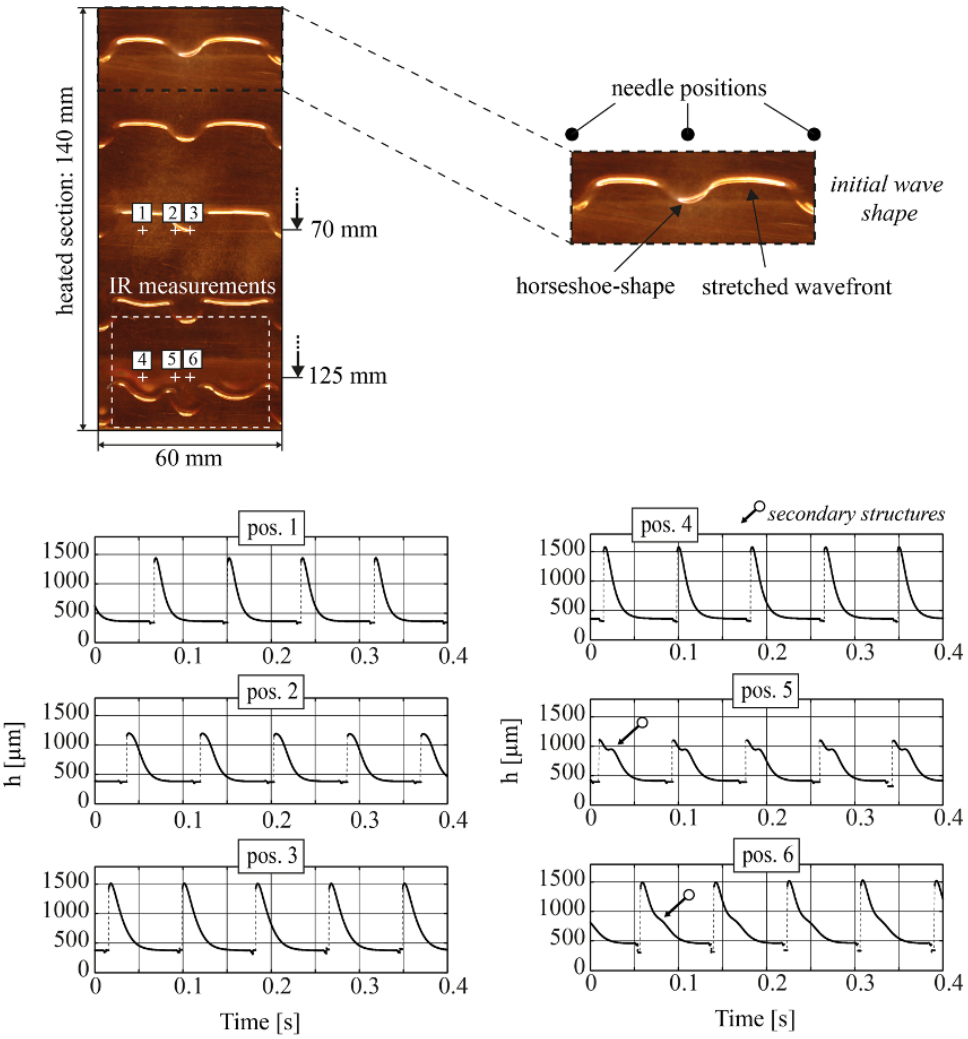

Fig. 4. Time traces of the film thickness at indicated positions on the heated section: The part of the heater that is shown corresponds to the most symmetrical center part of the falling film. IR measurement were conducted within the dashed area at the bottom of the picture.

wall temperature of 70 °C, the wave topology starts to deviate significantly from the isothermal case beyond the middle of the heated section. Thus, respective film thickness time traces from the entrance of the heated section are not shown.

In the center part of the heated section (pos. 1-3), the maximal height of the wave crest is found in the center of the horseshoe-shaped part (pos. 3). The minimal height of the wave crest is located besides the horseshoe-shaped part, where the wave front is not orientated normal to the flow direction (pos. 2). The part of the wave crest between two horseshoe structures is referred to as the "stretched wave front" [18]. In this part, the wave exhibits a strong two-dimensional character, for which good agreement between two-dimensional simulations and experimental results has been found [19]. Note that the missing measurement points in front of the main wave hump result from the limitation of the CCI to a maximum viewing angle.

From positions 1-3 to positions 4-6 significant deviations of the wave shape occur which can be associated to a reduced viscosity in the hotter near-wall region and to

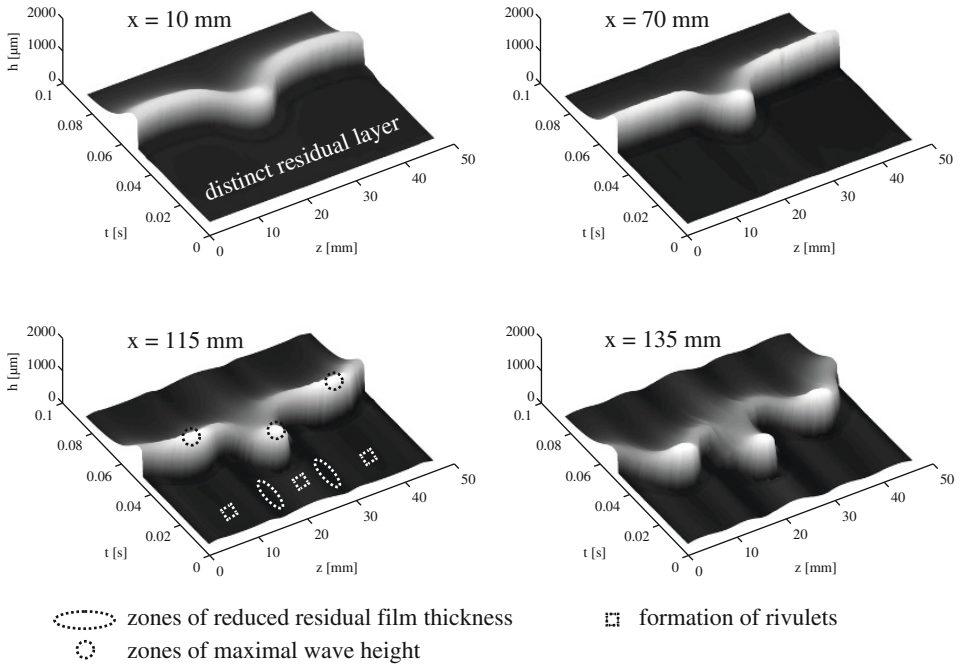

Fig. 5. Three-dimensional reconstructions of the film topology for the heated case: Note, that the images show temporal reconstructions at one respective streamwise position.

thermocapillary forces. The wave topology in the center of the horseshoe-shaped wave front (pos. 3 and 6) changes from a solitary wave structure with a distinct residual layer to a wave type exhibiting a secondary structure located inside the back of the wave as well as a reduced length of the residual layer. However, the thickness of the residual layer is found to increase slightly, while the maximum film thickness is less affected.

In the center of the stretched wave front, a significant increase in the height of the peak (pos. 1 and 4) occurs. This results in a local increase of the wave velocity as well as in the formation of secondary horseshoe-type structures, and consequently in a wave number doubling of the spanwise structures.

In the region of minimum wave height (pos. 2 and 5), a more distinct secondary structure inside the back of the wave is formed, which was associated with the break-up of the previously continuous wave front into separate staggered wave fronts [18].

Figure 5 illustrates the three-dimensional development of the film topology, measured at four streamwise locations. The top left picture shows the topology 10 mm downstream the entrance of the heater, where the wave is characterized by a continuous wave front. The wave topology at a position $x = 70$ mm downstream (top right picture) shows no significant deviations from the initial topology. However, the stretched wave front has changed from a slightly concave shape ($x = 10$ mm) to an almost straight shape, already revealing an increase in the relative wave velocity. At $x = 115$ mm, the form of the stretched wave has further changed to a convex shape with a significant increase of the center wave peak height due to lateral thermocapillary flows induced by a lateral modulation of the film thickness, hence of the surface temperature. For the same reason, the wave peak height in the center of the horseshoe structure exhibits a moderate growth in wave height in comparison to the initial wave height. The height of the wave crest between the two parts decreases,

resulting in a separation of the wave. Further, the thickness of the residual layer at this position decreases, leading to a spanwise modulation of the residual layer and the formation of rivulets. The spanwise positions of the rivulets coincide with positions of the wave crest maxima (dashed circles). The last picture, showing the topology at $x = 135\,\mathrm{mm}$, clearly reveals the wave number doubling and rivulet formation. Regularly spaced rivulets with large waves on top are separated by distinct troughs (dashed ovals). This corresponds to a state somewhere between a topology dominated by rivulets and a topology dominated by fully developed 3D waves, classified as regime II by Scheid et al. [20] in the context of the interaction of hydrodynamic and thermocapillary instabilities.

The evolution of the film topology is further examined through spanwise profiles around the wave crest (Fig. 6a) and along the residual film (Fig. 6b) at different streamwise positions (from $x = 10\,\mathrm{mm}$ to $x = 135\,\mathrm{mm}$ after the entrance of the heater). The film thickness profiles of the residual layer are evaluated 150 ms downstream the center peak of the respective horseshoe-shaped structure of the wave crest. The increase or decrease of the thickness is illustrated in the two bottom plots for distinct spanwise positions. Regarding the development of the wave crest (Fig. 6a), initial disturbances imposed by the excitation are reinforced by thermocapillary convection. The significant increase of the peak in the center of the horseshoe structure (from $1420\,\mu\mathrm{m}$ to $1520\,\mu\mathrm{m}$) and the center of the stretched wave front (from $1350\,\mu\mathrm{m}$ to $1580\,\mu\mathrm{m}$) is compensated by a strong decrease of the wave between these two positions (from $1200\,\mu\mathrm{m}$ to $980\,\mu\mathrm{m}$). Further, the width of the gap between the two peaks increases, reducing the spanwise expansion of the rivulet formed from the stretched wave front. Finally, the spanwise distribution of the wave peak height is characterized by two local maxima and two local minima in the range of the imposed wavelength.

The development of the film thickness at the three indicated positions (see bottom left plot) shows that the peak height in the center of the horseshoe structure is saturated. On the contrary, no saturation is found for the other two positions within the measurement range.

The spanwise profiles of the residual layer (Fig. 6b) show an almost constant thickness for $x = 10\,\mathrm{mm}$, however, with a slightly higher value in the area of the horseshoe-type structure. For all later profiles, a decrease of the average film thickness is found ($\Delta\bar{h}_{\mathrm{min}} \approx 30\,\mu\mathrm{m}$), which can be associated with the reduced viscosity in the near-wall region and the acceleration of the waves. This decrease in film thickness dominates the development of the wave topology in the residual layer approximately half way through the heated section. Beyond this point, the development of the topology is strongly dominated by thermocapillary forces leading to the development of a "cascade of structures" [2]. The origin of the thermocapillary induced spanwise modulations of the film thickness is found in the transition region between the horseshoe-shaped wavefront and the stretched wavefront. There, the lower height of the wave crest in combination with an approximately constant film thickness in the residual layer leads to a locally lower average film thickness in streamwise direction and consequently to locally higher surface temperatures again leading to spanwise shear stresses at the surface (further details are given in the next section).

From $x = 70\,\mathrm{mm}$ and onward, the spanwise profile of the residual layer is characterized by multiple distinct maxima and minima. Three local minima are found. First, in the center of the horseshoe structure, second, in the center of the stretched wave front, and third, between the two structures, which is also the global minimum. The two first mentioned local minima are associated to an additional transverse modulation of the rivulets, emerging at the position of maximum peak height. This modulation is found to be sustained in the area where the stretched wave front is located. The local maximum in the wave peak height is here preceded in streamwise

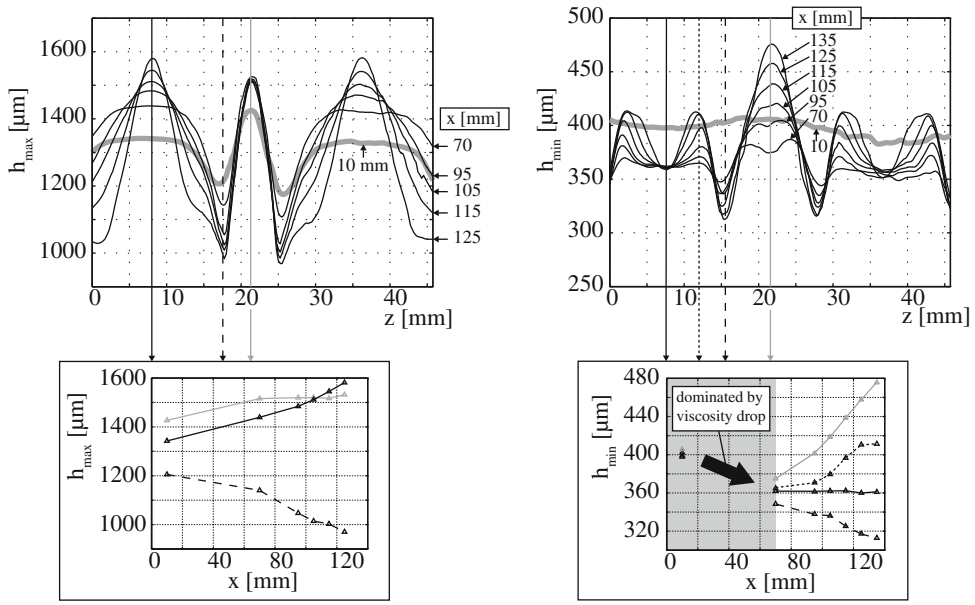

(a) Around the wave crest (b) Along the residual film

Fig. 6. Development of spanwise film thickness profiles over the expansion of the heating section. Initial thickness is depicted in bold gray. (a) Development of the wave peak height profile; (b) Development of the film thickness along the residual film. The pointwise development is illustrated at indicated cuts through the profiles. Residual film thickness profiles are evaluated 150 ms before the center peak of the horseshoe-shaped structure of the wave crest.

direction by a local minimum in the residual layer. On the contrary, in the area of the horseshoe structure, additional transverse modulations are suppressed, such that the local maximum in the wave peak height is preceded by a local maximum in the residual layer. The two rivulets which are previously found to emerge from wave number doubling are thus found to be different in their structure with respect to the residual layer. Similar to the development of the wave peak height, no saturation is found for the minimal film thickness in the investigated area (see bottom right plot), pointing at critical film thinning in the area of the global minima in film thickness.

The experimental observations agree well with the results obtained with the integral boundary layer model by Scheid et al. [20], where secondary rivulets between the main ones have been identified. The formation of a "cascade of structures" has also been identified in horizontal layers in the film thinning process before film rupture [2].

3.2 Evolution of surface temperature

The evolution of the surface temperature from $x = 95\,\mathrm{mm}$ to $x = 130\,\mathrm{mm}$ is shown in Fig. 7. In Fig. 7a three-dimensional thermograms of the surface are shown, whereby the flow direction is flipped, providing a better visibility of the thermal structures. The left plot depicts an instantaneous surface temperature distribution whereas the right plot shows the locally averaged temperature with an averaging time of ten seconds (2400 images). Temperature differences are given based on the mean surface temperature averaged over the entire investigated region. Note, that contrarily to the film

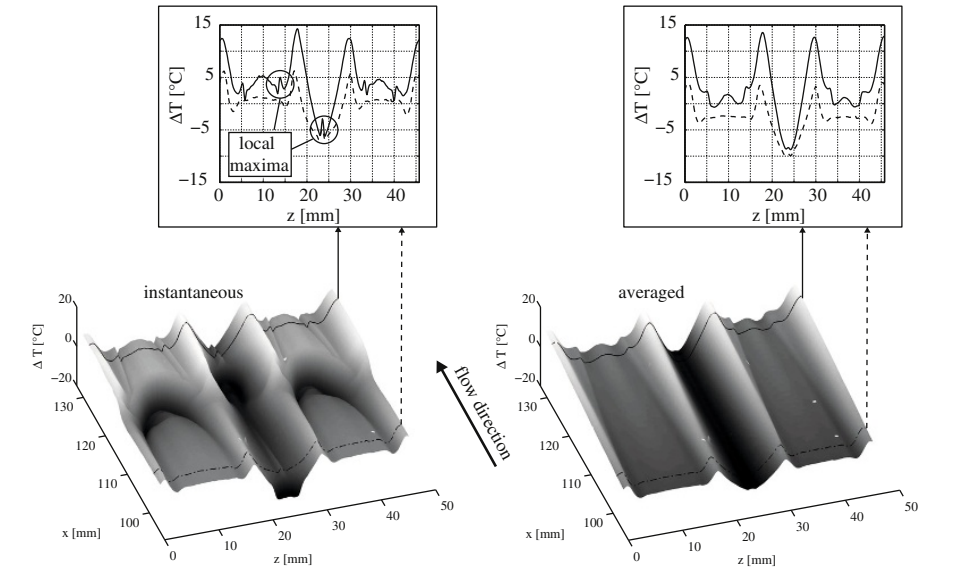

(a)

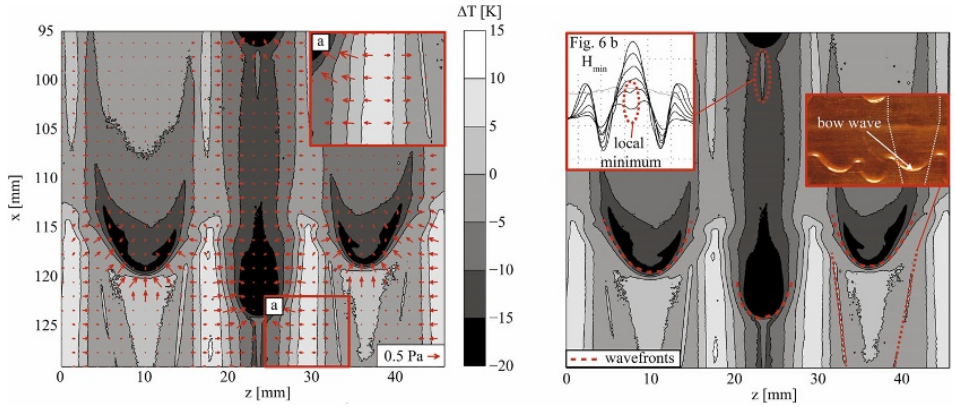

(b)

Fig. 7. Surface temperature measurements for $x = 95$–130 mm downstream the entrance of the heater: (a) instantaneous surface temperature distribution (left); surface temperature averaged over 10 s (right). Profiles are shown for indicated x-positions. (b) Entanglement of developing thermal structures and the development of the film's interfacial topology. Contour plots of the instantaneous surface temperature distribution in the given range are presented. The left plot illustrates interfacial shear stresses indicating the direction of thermocapillary convection. The right plot shows the emerging of thermal structures due to temporal developments of the wave topology.

thickness measurements (where the temporal development is given for one specific streamwise position), the surface temperature measurements are two-dimensional.

The instantaneous surface temperature distribution displays the same symmetry with respect to the imposed wavelength in spanwise direction as the plot of the film topology. However, compared to the wave topology in the residual layer, the surface

temperature exhibits more maxima and minima with steep gradients as shown by the two profiles. One local maximum is found in front of the center of the horseshoe structure at $z = 22\,\text{mm}$. A second localized structure is found on both sides of the stretched wave front at $z = 5\,\text{mm}$ and $z = 14\,\text{mm}$ (Fig. 7a left). These local small-scale temperature peaks are in the range of the uncertainty of the temperature measurements. Nevertheless, their occurrence in several independent measurements points to physical causes (see Fig. 7b right), while the magnitude of these peaks cannot be quantified with certainty.

The described thermal structures are also present in the average surface temperature distribution, however with less steep gradients. The two profiles at $x = 98\,\text{mm}$ and $x = 127\,\text{mm}$ reveal an increasing number of thermal structures as well as a strongly increasing temperature on both sides of the horseshoe structure (at $z = 19\,\text{mm}$ and $z = 29\,\text{mm}$), which form distinct hot strikes. The position of the hot strikes coincides with the position of the global minima in the wave peak height (see Fig. 6a), where the replenishing mechanism of the main wave hump is least pronounced. On the contrary, the surface temperature in the spanwise position of the horseshoe structure, despite the emerging of the local increase, does not change significantly corresponding to the local increase in film thickness (Figs. 6a,b).

Figure 7b provides a more detailed picture of the developing thermal structures. The left plot indicates shear stresses at the interface due to gradients in surface tension. The shear stress τ is evaluated through $\tau = \frac{\partial \sigma}{\partial T} \cdot \text{grad(T)}$ with σ denoting the surface tension coefficient and T denoting the local surface temperature. The vector field illustrates the direction of thermocapillary convection, revealing the feeding mechanism of the wave crest as well as the source of spanwise modulations in the residual layer, which is emphasized in insert (a). The developing hot strikes lead to spanwise flows, which locally amplify the film thinning process and induce the development of a cascade of structures as described with respect to the surface topology development (Fig. 6).

The right plot of Fig. 7b illustrates the connection between the development of the surface topology and the development of the additional local maxima with steep gradients, observed in the surface temperature distribution. The structures on both sides of the stretched wavefront develop towards the end of the investigated area and are of conically tapering form. This shape is apparent in the shown image and can be associated to the convergence of the stretched wave front (bow wave) to additional horseshoe-like structures in the wave number doubling process. This convergence is grounded in the strong increase of the local wave peak height and the corresponding acceleration of the center of the stretched wavefront. The causing effect of the local temperature maximum in front of the center of the horseshoe structure remains not explicitly revealed. The experimental data does not clearly indicate whether this thermal structure is caused by either the temporal spanwise modulation of the center rivulet as indicated in the shown insert or by local flow structures transferring hot fluid from the near-wall region to the interface. A reconstruction of the observed structures in numerical simulations could lead to necessary deeper insights into flow dynamics within the liquid film in the region of interest.

4 Conclusion

Interactions of wave dynamics and thermocapillary effects have been experimentally investigated for a heated vertical falling liquid film. In particular, a case of regularly excited solitary-type waves exhibiting symmetry in spanwise and streamwise direction is presented as a benchmark for the validation of future related numerical simulations. The development of the surface topology has been determined through chromatic

confocal imaging and the surface temperature distribution has been analyzed through infrared thermography.

A wave number doubling process of spanwise perturbations within the wave crest has been observed, leading to a wave topology characterized by horseshoe structures separated by distinct troughs. Simultaneously, the development of thermal structures in the initially plain inter-wave region is illustrated, showing the emerging of rivulets with additional transverse modulations at spanwise positions of the horseshoe structures. The transverse modulation within emerging rivulets is seen to be either suppressed or sustained throughout the expansion of the heater.

The rivulet formation is also visible in the surface temperature distribution through the development of distinct hot strikes in the region of decreasing film thickness between consecutive spanwise rivulets, amplifying the local critical film thinning process. Additional thermal structures in the interfacial temperature distribution are partly associated to the development of the wave topology. Particularly, the development of additional horseshoe structures in the spanwise wave number doubling process leads to v-shaped thermal structures, also visible in the averaged interfacial film temperature. Deeper insights into the emerging of thermal structures and interactions with wave dynamics are expected from the comparison to related numerical simulations.

Funding for M.R. was provided by the HITEC (Helmholtz Interdisciplinary Doctoral Training in Energy and Climate Research) graduate school. Funding for W.R. was provided by DFG (Deutsche Forschungsgemeinschaft) under grant number KN-764-3-2. B. S. thanks the F.R.S.-FNRS for financial support as well as the Belgian Science Policy Office under the IAP 7/38 MicroMAST project. B.S. and W.R. also acknowledge the financial support of EU-FP7 ITN MULTIFLOW.

References

1. S.V. Alekseenko, V.E. Nakoryakov, B.G. Pokusaev, *Wave Flow of Liquid Films* (Begell House, 1994)
2. W. Boos, A. Thess, Phys. Fluids, 11 (1999)
3. J. Cohen-Sabban, J. Gaillard-Groleas, P.-J. Crepin, Opt. Metrol. Roadmap Semiconduct. Opt. Data Storage Indust. II **4449**(1), 178 (2001)
4. G.F. Dietze, Flow separation in falling liquid films, Ph.D. thesis, RWTH Aachen, 2010
5. G.F. Dietze, F. Al-Sibai, R. Kneer, J. Fluid Mech. **637**, 73 (2009)
6. G.F. Dietze, W. Rohlfs, K. Nährich, B. Scheid, J. Fluid Mech. **743**, 75 (2014)
7. S.W. Joo, S.H. Davis, S.G. Bankoff, J. Fluid Mech. **230**, 117 (1991)
8. O.A. Kabov, J.C. Legros, I.V. Marchuk, B. Scheid, Fluid Dyn. **36**, 521 (2001)
9. O.A. Kabov, B. Scheid, I.A. Sharina, J.C. Legros, Int. J. Ther. Sci. **41**, 664 (2002)
10. S. Kalliadasis, C. Ruyer-Quil, B. Scheid, M.G. Velarde, *Falling Liquid Films* (Springer London Dordrecht Heidelberg, New York, 2012)
11. V.V. Lel, Hydrodynamik und Wärmeübergang laminar-welliger Rieselfilme, Ph.D. thesis, RWTH Aachen, 2007
12. V.V. Lel, F. Al-Sibai, R. Kneer, Exper. Fluid. **39**, 856 (2005)
13. V.V. Lel, A. Kellermann, G. Dietze, R. Kneer, A.N. Pavlenko, Exper. Fluids **44**, 341 (2008)
14. P. Nosoko, P. N. Yoshimura, T. Nagata, K. Oyakawa, Chem. Eng. Sci. **51**(5), 725 (1996)
15. C.D. Park, T. Nosoko, AIChE J. **49**(11), 2715 (2003)
16. B. Ramaswamy, S. Krishnamoorthy, S.W. Joo, J. Comput. Phys. **131**, 70 (1997)
17. W. Rohlfs, G. Dietze, H.D. Haustein, R. Kneer, Eur. Phys. J. Special Topics **219**, 111 (2013)
18. W. Rohlfs, G. Dietze, H.D. Haustein, O.Y. Tsvelodub, R. Kneer, Exper. Fluids **53**, 1045 (2012)

19. W. Rohlfs, H.D. Haustein, G.F. Dietze, R. Kneer, *Proceedings of the 6th International Berlin Workshop – IBW3 on Transport Phenomena with Moving Boundaries*, Nov. 24-25, 2011, Berlin, VDI Fortschritts-Bericht VDI Reihe 3, Verfahrenstechnik 929, Düsseldorf VDI-Verlag
20. B. Scheid, S. Kalliadasis, C. Ruyer-Quil, P. Colinet, Phys. Rev. E **78**, 066311 (2008)
21. B. Scheid, C. Ruyer-Quil, P. Manneville, J. Fluid Mech. **562**, 183 (2006)
22. P.M.J. Trevelyan, B. Scheid, C. Ruyer-Quil, S. Kalliadasis, J. Fluid Mech. **592**, 295 (2007)
23. D.W. Zhou, T. Gambaryan-Roisman, P. Stephan, J. Heat Trans. **33**(2), 273 (2009)